ROYAL SOCIETY
OF CHEMISTRY

COMMUNICATION

Check for updates

Controlled synthesis of GaSe microbelts for high-gain photodetectors induced by the electron trapping effect†

Chun-Yan Wu, [iD] Huinan Zhu, Ming Wang, Jingwei Kang, Chao Xie,* Li Wang and Lin-Bao Luo [iD] *

GaSe microbelts were successfully synthesized using Ga/Ga₂Se₃ as the precursor mixture, where excess Ga was required to serve as the metal catalyst. Meanwhile, a spontaneously oxidized surface amorphous oxide (GaO$_x$) layer formed, which induced a built-in electric field perpendicular to the surface. Benefiting from this effect, a GaSe microbelt-based photodetector attained a high responsivity of $\sim$3866 A W^{-1} and a photoconductive gain of up to $\sim$1.06 $\times$ 10^4. This study sheds light on the controlled synthesis of microstructures and provides a device design concept for high-performance micro/nano optoelectronics.

As a typical group III–VI layered semiconductor material, GaSe has an indirect band gap of $\sim$2.11 eV and a direct band gap only 25 meV higher, whose small difference makes the transfer of excitons very easy.[1,2] By the same token, this material presents prominent nonlinear optical properties, which enable its application in many fields such as optoelectronics,[3–5] nonlinear optics,[6] and terahertz (THz) generation.[7] Bulk GaSe is formed by stacking close-packed Se–Ga–Ga–Se planar quaternary layers along the *c*-axis bonded together by weak interplanar van der Waals interactions. Therefore, similar to other two-dimensional (2D) materials, mono- or few-layer GaSe can show unique electronic, optical, chemical and mechanical properties arising from the self-terminated and dangling-bond free surface as well as the layer-dependent physical properties. Moreover, the mechanical and electronic properties may also be affected by the application of an electric potential, which may change the surface energy, promoting nucleation of plastic shear and development of various defects.[8,9] The above features render GaSe a perfect candidate for next generation electronic and optoelectronic devices.[10–13] More intriguingly, GaSe exhibits the rarely reported p-type electrical characteristics among various layered semiconductors,[14] which facilitates the fabrication of van der Waals p–n heterojunctions and is also helpful for integration into high-performance functional devices as well as logic circuits.[15,16]

School of Electronic Science and Applied Physics, Hefei University of Technology, Hefei, Anhui 230009, P. R. China. E-mail: chao.xie@hfut.edu.cn, luolb@hfut.edu.cn
† Electronic supplementary information (ESI) available. See DOI: 10.1039/d0tc01120g

The weak van der Waals interactions between two neighboring layers of GaSe make it possible to obtain mono- or few-layer GaSe structures from its bulk crystals through mechanical exfoliation.[17] For instance, Late *et al.*[14] first demonstrated the fabrication of a field effect transistor (FET) based on a mechanically exfoliated GaSe ultrathin layer, giving a mobility of 0.6 cm^2 V^{-1} s^{-1}. Furthermore, Hu *et al.*[5] reported a photodetector designed using solvent or mechanically cleaved GaSe nanosheets, which shows a high responsivity of 2.8 A W^{-1} and a high external quantum efficiency (EQE) of 1367%. Afterwards, by shrinking the electrode space distance down to 290 nm, the responsivity of a layered GaSe based photodetector was significantly enhanced to 5000 A W^{-1}.[18] Nevertheless, despite the progress, the inherent limitations such as poor reproducibility and low yield of mechanically exfoliated layers still restrict the further development of GaSe-based electronics and optoelectronics, especially when the devices reach scalable size.

In contrast, the vapor deposition technique shows prominent advantages for mass production of GaSe crystals with high yields.[19–21] For example, Yuan *et al.*[22] presented the wafer-scale growth of GaSe thin films by molecular beam epitaxy. Using the pulsed laser deposition method, Mahjouri-Samani *et al.*[23] reported the stoichiometric transfer of GaSe nanosheet networks. In addition, the controlled synthesis of 2D GaSe crystals on mica has been realized by virtue of van der Waals epitaxy.[24] To compensate for the volatilization of Se during thermal evaporation, precursors such as Ga₂Se₃[25] or mixtures (*e.g.*, GaSe/Ga₂Se₃[26] or Ga/Ga₂Se₃[27]) have also been employed for growing GaSe crystals in some reports. Due to the different vapor pressures of the precursor materials, unexpected impurities or defects are inevitably introduced into the resultant products. However, the effect of these impurities or defects on the optoelectronic properties of the GaSe crystals is unclear and further study is essentially required.

Herein, we report the controlled synthesis of GaSe microstructures using Ga/Ga₂Se₃ as the precursor mixture. In particular, GaSe microbelts on mass scale are obtained when excess Ga is employed. A single GaSe microbelt is assembled into a photodetector, which reveals a high responsivity and photoconductive gain of $\sim$3866 A W^{-1} and $\sim$1.06 $\times$ 10^4, respectively, at 3 V bias,

under 450 nm light illumination (9.47 μW cm^{-2}). The high gain can be mainly related to a built-in electric field formed between the GaSe microbelt and the surface amorphous oxide (GaO$_x$) layer arising from the spontaneous oxidation of absorbed Ga residues. Upon illumination, the photoinduced electrons are quickly swept into the GaO$_x$ layer by the built-in electric field, and holes are left within the microbelts, which significantly reduces carrier recombination. While electrons are trapped in the GaO$_x$ layer, holes are transported and recirculated many times until being recombined. The above process thus gives rise to a large photoconductive gain. It is believed that the present study will be inspiring for further studies on the controlled preparation of microstructures and design of high-performance micro/nano optoelectronics.

The GaSe microstructures were synthesized in a horizontal tube furnace using a Ga/Ga$_2$Se$_3$ precursor mixture and the details are provided in the ESI.† The proportion of the mixture precursors is a pivotal parameter for material synthesis. Therefore, precursor mixture with different Ga : Ga$_2$Se$_3$ proportions (*e.g.*, 0:1, 1:1, 2:1 and 3:1 in molar ratio) were employed, and the corresponding FESEM images of the products are shown in Fig. 1a–d, respectively. Apparently, only irregularly aggregated nanoparticles were observed when a pure Ga$_2$Se$_3$ precursor was used (Fig. 1a). However, when we employed an equimolar mixture of Ga/Ga$_2$Se$_3$, a uniform layer of microsheet networks could be formed (Fig. 1b). These microsheets have a size of 20–50 μm and thickness less than 1 μm, showing remarkable anisotropic growth of layered materials. When further increasing the Ga content (Ga : Ga$_2$Se$_3$ = 2:1), one dimensional (1D) microstructures (microbelts and microrods) began to show up (Fig. 1c). Finally, massive microbelts with a width of 1–2 μm and length up to several centimeters were obtained when the Ga : Ga$_2$Se$_3$ = 3:1 precursor mixture was used (Fig. 1d). Careful observation found that sphere particles existed on the tips of some microbelts. In addition, microbelts with saw-toothed edges or zigzag morphologies could also be observed, which should be ascribed to the low surface-interfacial energy of Ga liquid droplets.[28] These droplets are very sensitive to perturbation and may change the growth direction of the microbelts constantly during growth.
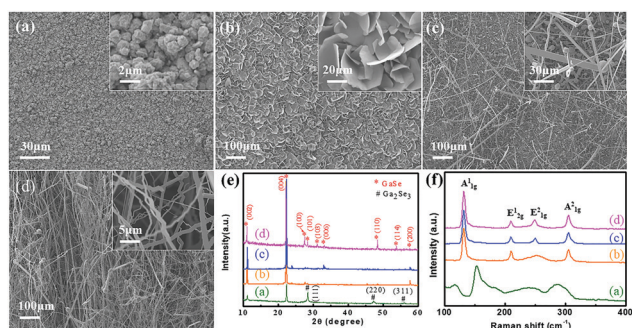
Fig. 1e depicts the XRD patterns of the GaSe microstructures prepared using different precursor mixtures. It was found that when a pure Ga$_2$Se$_3$ precursor was used, a face-centered cubic Ga$_2$Se$_3$ crystal phase (JCPDS card No. 05-0724) and hexagonal GaSe crystal phase (JCPDS card No. 78-1927) coexisted in the product. Nevertheless, GaSe crystals without evident impurities were obtained when precursor mixtures with equimolar Ga/Ga$_2$Se$_3$ or excess Ga were employed. Furthermore, the Raman spectra of GaSe crystals showed four prominent peaks at 131.9 cm^{-1}, 210.3 cm^{-1}, 250.1 cm^{-1} and 305.9 cm^{-1} (Fig. 1f), which could be assigned to the A$_{1g}^1$, E$_{2g}^1$, E$_{1g}^2$ and A$_{1g}^2$ phonon vibrational modes of GaSe crystal, respectively.[14] In particular, the A$_{1g}$ mode corresponded to the out-of-plane vibration of the Se–Ga–Ga–Se lattice, while E$_{2g}$ and E$_{1g}$ corresponded to the in-plane vibration.

Therefore, we believe that excess Ga plays a vital role in the growth of GaSe microbelts. In fact, GaSe vapor would be first formed according to the equation Ga + Ga$_2$Se$_3$ → GaSe, which was then transferred by the carrier gas downstream of the tube and deposited onto the SiO$_2$/Si substrate due to a decreased temperature. In the case of equimolar Ga/Ga$_2$Se$_3$ precursors, all Ga was involved in the reaction. Therefore, there was no metallic catalyst, and the vapor–solid (VS) mechanism dominated the growth of GaSe crystals. Due to the layered structure, the GaSe nucleus tended to incorporate atoms at the edges and thus grew into microsheets (Fig. 1b). In contrast, for the precursor mixture with excess Ga, the extra Ga would condense on the substrate and served as a catalyst to induce the growth of 1D microstructures *via* the vapor–liquid–solid (VLS) mechanism. The above hypothesis can be verified by the elemental mapping taken from an individual microbelt with a particle on the tip. As shown in Fig. S1 (ESI†), only the Ga element could be found at the tip while both Ga and Se elements distributed uniformly along the whole microbelt, indicating that the metallic Ga particle served as a catalyst for the growth of the GaSe microbelt.

The GaSe microbelts were further characterized by using TEM and the images are shown in Fig. 2a–c. A HRTEM image taken from the edge of a single GaSe microbelt (Fig. 2b) disclosed well-defined 2D lattice fringes with an interplanar spacing of 0.187 nm, corresponding to the (110) lattice plane of hexagonal GaSe. Combining with the fast Fourier transformation (FFT) pattern (inset in Fig. 2b), we can deduce that the microbelt grew along the [110] direction and formed a flat surface parallel to the (001) plane, which agreed well with the preferential growth direction in the XRD pattern as well (Fig. 1e). The above results also confirmed the layered structure of the as-synthesized GaSe microbelts. In addition, it should be noted that a thin amorphous layer with a thickness of ∼3 nm (marked by the red dotted line) could be clearly observed at the surface of the microbelt, as depicted by the HRTEM image. An EDS spectrum (inset in Fig. 2a) and the elemental mapping (Fig. 2c) also showed the existence of a small amount of O element in the microbelt.

To unveil the origin of the O element, XPS spectra were then recorded on an as-synthesized GaSe microbelt and another microbelt that had been treated with Ar$^+$ ion etching for 30 s to remove the surface amorphous layer. As displayed in Fig. 2d, the slightly broadened Ga 3d peak of the untreated sample

Fig. 1 FESEM images of the as-synthesized products using different proportions of precursor mixtures: (a) Ga : Ga$_2$Se$_3$ = 0:1, (b) Ga : Ga$_2$Se$_3$ = 1:1, (c) Ga : Ga$_2$Se$_3$ = 2:1, and (d) Ga : Ga$_2$Se$_3$ = 3:1. Insets show the corresponding magnified FESEM images. (e) XRD patterns and (f) Raman spectra of different products.

5376 | *J. Mater. Chem. C*, 2020, **8**, 5375–5379

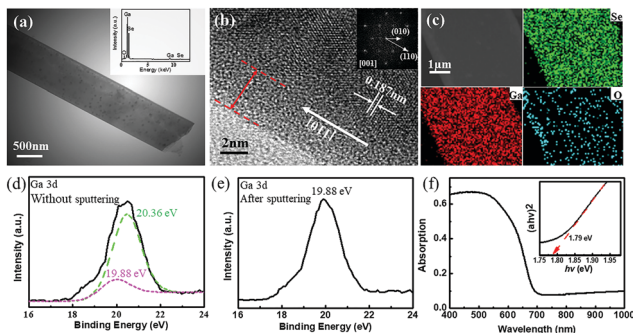This journal is © The Royal Society of Chemistry 2020

Fig. 2 (a) TEM image of a single GaSe microbelt. Inset shows the EDS spectrum. (b) HRTEM image taken of the edge of the GaSe microbelt. Inset shows the corresponding fast Fourier transformation (FFT) pattern. (c) Elemental mapping of the GaSe microbelt. Ga 3d core level of (d) the as-synthesized GaSe microbelt and (e) the sample treated with Ar$^+$ ion etching for 30 s. (f) Optical absorption spectrum of the GaSe microbelts. Inset shows the corresponding $(\alpha h v)^2 - h v$ plot.

could be divided into two peaks located at 19.88 eV and 20.36 eV, which were indexed to Ga 3d in Ga_2Se_3 and Ga 3d in Ga_2O_3, respectively.[29] However, only the Ga 3d peak corresponding to Ga_2Se_3 (situated at 19.88 eV) appeared at the XPS spectrum obtained from the treated sample. Therefore, based on the above results, it was reasonable to state that the surface amorphous layer is a layer of GaO_x, which was formed through spontaneous oxidation of the residual Ga absorbed onto the surface of the microbelt, when exposed to air.

Fig. 2f presents the absorption spectrum of the GaSe microbelts, from which a strong absorption in the visible spectrum region with an evident absorption edge located at about 700 nm was observed. In addition, from the relationship of $(\alpha h v)^2 - h v$, the optical band gap was deduced to be about 1.78 eV (the inset in Fig. 2(f)), which was comparable to that of bulk GaSe crystals.[1]

By using an individual GaSe microbelt as the building block, a two-terminal photodetector was then constructed (Fig. 3a) and a representative SEM image is shown as an inset in Fig. 3b. Fig. 3b plots the current–voltage (I–V) curves of the device
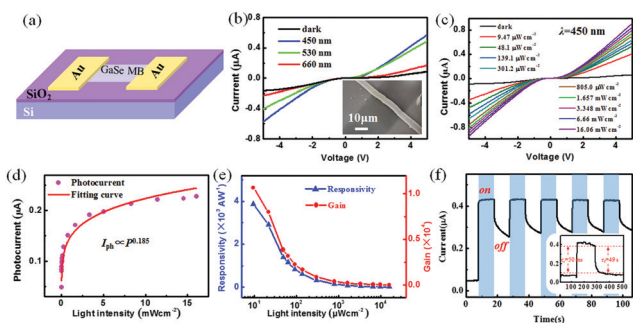
measured in the dark and upon light illumination. Apparently, the device showed a pronounced photoresponse to all illuminations and the photocurrent increased gradually with the decrease in light wavelength. The spectral response recorded at a fixed light intensity in the wavelength range of 400–1000 nm is plotted in Fig. S2 (ESI†), which was also consistent with the absorption spectrum shown in Fig. 2f. It was also found that all the curves exhibited a slightly non-linear behavior, which was likely caused by the presence of an amorphous thin layer between the metal electrodes and the microbelt.

The above photoresponse depended strongly on the incident light intensity. Fig. 3c presents the I–V curves under 450 nm illumination with different light intensities. Clearly, it could be observed that the photocurrent increased monotonously with the increase in the light intensity (Fig. 3c). In particular, the photocurrent exhibited a relatively rapid increase from 0.05 µA to 0.19 µA when the light intensity rose from 9.47 µW cm^{-2} to 3.348 mW cm^{-2}, while further increasing the light intensity from 3.348 to 16.06 mW cm^{-2} only led to a relatively slow increase of photocurrent from 0.19 µA to 0.23 µA. Such a relationship was reasonable since more electron–hole pairs would be excited upon illumination with a stronger intensity, giving rise to a higher photocurrent. Additionally, the dependence of photocurrent on light intensity could be further fitted using a widely employed power law: $I_{ph} \sim P^\theta$, where I_{ph} is defined as the net photocurrent ($I_{ph} = I_{light} - I_{dark}$) and the exponent θ is an empirical value reflecting the recombination of the photocarriers.[30] As shown in Fig. 3d, a low θ value of only 0.185 was obtained. The large deviation from the ideal value ($\theta = 1$) indicated the presence of a strong recombination loss in the present photodetector, especially at higher light intensity.[31]

To quantitatively assess the device performance, two key performance parameters, responsivity (R) and specific detectivity ($D^\star$), were calculated according to the following equations[32]

$$R\ (A\ W^{-1}) = \frac{I_{ph}}{SP_{in}} = \eta\left(\frac{\lambda q}{hc}\right)G \text{ and } D^* = R\sqrt{\frac{S}{2qI_d}}.$$ Based on

the above equations and parameters, R and $D^\star$ reached the values of $\sim$3866 A W^{-1} and $\sim$2.4 × 10^{14} Jones at 3 V under the light intensity of 9.47 µW cm^{-2}, respectively, which were much higher than those of most GaSe nanostructure-based photodetectors mentioned in previous studies (see Table S1, ESI†).[25,27] In fact, a higher responsivity can be obtained by simply increasing the operational bias voltage (Fig. 4a) because a larger bias can accelerate the transfer of holes, leading to a higher photocurrent. Furthermore, the value of G was deduced to be $\sim$1.06 × 10^4 by assuming 100% internal quantum efficiency. In addition, both R and G declined gradually as the light intensity increased (Fig. 3e), which again verified the existence of recombination loss in the photodetector. Upon light irradiation with a higher intensity, the activity of photocarrier recombination would be intensified because of the increased concentration of charge carriers in the microbelt.

Intrinsically, a photoconductor has no photoconductive gain or at least no high photoconductive gain.[33] So, the high gain of the present photodetector should be ascribed to other mechanisms. As mentioned above, the as-prepared GaSe microbelts

Fig. 3 (a) Schematic illustration of the single GaSe microbelt-based photodetector. (b) Current–voltage (I–V) curves of the photodetector measured in the dark and upon 450, 530, and 660 nm illumination at the light intensity of 130 µW cm^{-2}. Inset shows the SEM image of a typical device. (c) I–V curves of the photodetector under 450 nm illumination with varied light intensities. (d) Photocurrent as a function of light intensity. (e) Responsivity and gain as a function of light intensity (f) Time-dependent photoresponse of the photodetector at a bias voltage of 3 V.
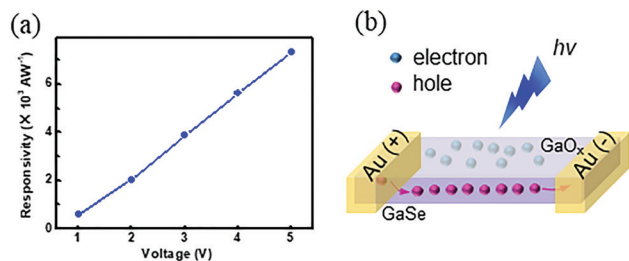
Fig. 4 (a) Responsivity of the single GaSe microbelt-based photodetector under different bias voltages. (b) Schematic of the charge carrier distribution in the photodetector based on a single GaSe microbelt with an outer GaO$_x$ layer.

were encapsulated with a thin GaO$_x$ layer. Therefore, due to the n-type electrical characteristics of the GaO$_x$ layer[34] and the p-type characteristics of the GaSe microbelt (Fig. S3, ESI†), a built-in electric field perpendicular to the surface of the microbelt would be formed near the interface of the GaSe microbelt/GaO$_x$ layer. When an incident light with photon energy larger than the band gap of GaSe is applied, a large number of electron–hole pairs would be generated within the microbelt. Subsequently, the electrons were quickly swept into the outer GaO$_x$ layer with the help of the built-in electric field and got trapped there, while the holes were left within the microbelt (Fig. 4b). The spatial separation of electrons and holes significantly reduced the carrier recombination activity. At the same time, driven by the external bias, the holes transferred fast and recirculated multiple times along the microbelt channel before recombination, which gave rise to a high photoconductive gain.[35,36] Note that the holes could be efficiently collected by the metal electrodes through the tunneling mechanism due to the ultrathin thickness of the GaO$_x$ layer.

Finally, the response speed of the GaSe microbelt-based photodetector was studied. Fig. 3f presents the time-dependent photoresponse of the device to pulsed 450 nm illumination, showing relatively good stability and repeatability. The rise and fall times were estimated to be 50 ms and 49 s, respectively, from a single magnified response curve. The long fall time suggested a slow recovery process of the channel current after switching off the light illumination, which was likely caused by the spatial separation of electrons and holes by the built-in electric field.[37]

In summary, we have presented the successful synthesis of GaSe microbelts on mass scale using a mixed precursor of Ga/Ga$_2$Se$_3$. The excess Ga serving as a metal catalyst was of vital importance for the morphology and yield of the resultant products. A photodetector composed of an individual GaSe microbelt showed a large responsivity of ∼3866 A W^{-1}, along with a high photoconductive gain of ∼1.06 × 10^4, at a bias voltage of 3 V under 450 nm light irradiation. Because of the spontaneous oxidation of the absorbed Ga residues, an amorphous GaO$_x$ thin layer was formed around the microbelt, which induced a built-in electric field near the interface of the microbelt and the GaO$_x$ layer. This built-in electric field could rapidly separate photogenerated electrons and holes within the microbelt and drive electrons into the GaO$_x$ layer, which greatly depressed the recombination of photocarriers. While the electrons were trapped in the GaO$_x$ layer, the holes left within the microbelt transferred and recirculated many times driven by the external bias voltage, giving rise to a high photoconductive gain. This work will be helpful for guiding the design of high-performance micro/nano optoelectronic devices.

Conflicts of interest

There are no conflicts to declare.

Acknowledgements

Notes and references

1 V. Capozzi and M. Montagna, *Phys. Rev. B: Condens. Matter Mater. Phys.*, 1989, **40**, 3182.
2 X. Zhou, J. X. Cheng, Y. B. Zhou, T. Cao, H. Hong, Z. M. Liao, S. W. Wu, H. L. Peng, K. H. Liu and D. P. Yu, *J. Am. Chem. Soc.*, 2015, **137**, 7994.
3 H. Huang, P. Wang, Y. Q. Gao, X. D. Wang, T. Lin, J. L. Wang, L. Liao, J. L. Sun, X. J. Meng, Z. M. Huang, X. S. Chen and J. H. Chu, *Appl. Phys. Lett.*, 2015, **107**, 143112.
4 S. D. Lei, L. H. Ge, Z. Liu, S. Najmaei, G. Shi, G. You, J. Lou, R. Vajtai and P. M. Ajayan, *Nano Lett.*, 2013, **13**, 2777.
5 P. A. Hu, Z. Z. Wen, L. F. Wang, P. H. Tan and K. Xiao, *ACS Nano*, 2012, **6**, 5988.
6 W. J. Jie, X. Chen, D. Li, L. Xie, Y. Y. Hui, S. P. Lau, X. D. Cui and J. H. Hao, *Angew. Chem., Int. Ed.*, 2015, **54**, 1185.
7 K. R. Allakhverdiev, M. Ö. Yetis, S. Özbek, T. K. Baykara and E. Y. Salaev, *Laser Phys.*, 2009, **19**, 1092.
8 S. V. Konovalov, V. I. Danilov, L. B. Zuev, R. A. Filip'ev and V. E. Gromov, *Phys. Solid State*, 2007, **49**, 1457.
9 L. B. Zuev, V. I. Danilov, S. V. Konovalov, R. A. Filip'ev and V. E. Gromov, *Phys. Solid State*, 2009, **51**, 1137.
10 M. Chhowalla, H. S. Shin, G. Eda, L.-J. Li, K. P. Loh and H. Zhang, *Nat. Chem.*, 2013, **5**, 263.
11 C. Xie, C. Mak, X. M. Tao and F. Yan, *Adv. Funct. Mater.*, 2017, **27**, 1603886.
12 B. Peng, P. KailianAng and K. P. Loh, *Nano Today*, 2015, **10**, 128.
13 Z. Zheng, L. Gan, H. Li, Y. Ma, Y. Bando, D. Golberg and T. Zhai, *Adv. Funct. Mater.*, 2015, **25**, 5885.
14 D. J. Late, B. Liu, J. J. Luo, A. Yan, H. S. S. R. Matte, M. Grayson, C. N. R. Rao and V. P. Dravid, *Adv. Mater.*, 2012, **24**, 3549.
15 N. Zhou, R. Y. Wang, X. Zhou, H. Y. Song, X. Xiong, Y. Ding, J. T. Lü, L. Gan and T. Y. Zhai, *Small*, 2018, **14**, 1702731.

5378 | *J. Mater. Chem. C*, 2020, **8**, 5375–5379

This journal is © The Royal Society of Chemistry 2020

16 X. F. Li, M.-W. Lin, J. H. Lin, B. Huang, A. A. Puretzky, C. Ma, K. Wang, W. Zhou, S. T. Pantelides, M. F. Chi, I. Kravchenko, J. Fowlkes, C. M. Rouleau, D. B. Geohegan and K. Xiao, *Sci. Adv.*, 2016, **2**, e1501882.

17 D. Bercha, K. Rushchanskii, L. Y. Kharkhalis and M. Sznajder, *Condens. Matter Phys.*, 2000, **3**, 749.

18 Y. Cao, K. Cai, P. Hu, L. Zhao, T. Yan, W. Luo, X. Zhang, X. Wu, K. Wang and H. Zheng, *Sci. Rep.*, 2015, **5**, 8130.

19 H. Cai, E. Soignard, C. Ataca, B. Chen, C. Ko, T. Aoki, A. Pant, X. Q. Meng, S. X. Yang, J. Grossman, F. D. Ogletree and S. Tongay, *Adv. Mater.*, 2016, **28**, 7375.

20 X. F. Li, L. Basile, B. Huang, C. Ma, J. Lee, I. V. Vlassiouk, A. A. Puretzky, M.-W. Lin, M. Yoon, M. F. Chi, J. C. Idrobo, C. M. Rouleau, B. G. Sumpter, D. B. Geohegan and K. Xiao, *ACS Nano*, 2015, **9**, 8078.

21 Y. B. Zhou, B. Deng, Y. Zhou, X. B. Ren, J. B. Yin, C. H. Jin, Z. F. Liu and H. L. Peng, *Nano Lett.*, 2016, **16**, 2103.

22 X. Yuan, L. Tang, S. S. Liu, P. Wang, Z. G. Chen, C. Zhang, Y. W. Liu, W. Y. Wang, Y. C. Zou, C. Liu, N. Guo, J. Zou, P. Zhou, W. D. Hu and F. X. Xiu, *Nano Lett.*, 2015, **15**, 3571.

23 M. Mahjouri-Samani, R. Gresback, M. K. Tian, K. Wang, A. A. Puretzky, C. M. Rouleau, G. Eres, I. N. Ivanov, K. Xiao, M. A. McGuire, G. Duscher and D. B. Geohegan, *Adv. Funct. Mater.*, 2014, **24**, 6365.

24 Y. B. Zhou, Y. F. Nie, Y. J. Liu, K. Yan, J. H. Hong, C. H. Jin, Y. Zhou, J. B. Yin, Z. F. Liu and H. L. Peng, *ACS Nano*, 2014, **8**, 1485.

25 X. Xiong, Q. Zhang, X. Zhou, B. Jin, H. Q. Li and T. Y. Zhai, *J. Mater. Chem. C*, 2016, **4**, 7817.

26 X. F. Li, M.-W. Lin, A. A. Puretzky, J. C. Idrobo, C. Ma, M. F. Chi, M. Yoon, C. M. Rouleau, I. I. Kravchenko, D. B. Geohegan and K. Xiao, *Sci. Rep.*, 2014, **4**, 5497.

27 L. P. Tang, Z. X. Zhao, S. P. Yuan, T. F. Yang, B. X. Zhou and H. Zhou, *J. Phys. Chem. Solids*, 2018, **118**, 186.

28 H. L. Peng, S. Meister, C. K. Chan, X. F. Zhang and Y. Cui, *Nano Lett.*, 2007, **7**, 199.

29 H. Iwakuro, C. Tatsuyama and S. Ichimura, *Jpn. J. Appl. Phys.*, 1982, **21**, 94–99.

30 L. H. Zeng, S. H. Lin, Z. J. Li, Z. X. Zhang, T. F. Zhang, C. Xie, C. H. Mak, Y. Chai, S. P. Lau, L. B. Luo and Y. H. Tsang, *Adv. Funct. Mater.*, 2018, **28**, 1705970.

31 Y. Shao, Z. Xiao, C. Bi, Y. Yuan and J. Huang, *Nat. Commun.*, 2014, **5**, 5784.

32 C. Xie, C. K. Liu, H. L. Loi and F. Yan, *Adv. Funct. Mater.*, 2019, DOI: 10.1002/adfm.201903907.

33 Y. P. Dan, X. Y. Zhao, K. X. Chen and A. Mesli, *ACS Photonics*, 2018, **5**, 4111.

34 Y. Qin, S. B. Long, Q. M. He, H. Dong, G. Z. Jian, Y. Zhang, X. H. Hou, P. J. Tan, Z. F. Zhang, Y. J. Lu, C. X. Shan, J. L. Wang, W. D. Hu, H. B. Lv, Q. Liu and M. Liu, *Adv. Electron. Mater.*, 2019, **5**, 1900389.

35 Q. H. Zhao, W. Wang, F. Carrascoso-Plana, W. Q. Jie, T. Wang, A. Castellanos-Gomez and R. Frisenda, *Mater. Horiz.*, 2020, **7**, 252.

36 Z. Chen, Z. Cheng, J. Wang, X. Wan, C. Shu, H. K. Tsang, H. P. Ho and J.-B. Xu, *Adv. Opt. Mater.*, 2015, **3**, 1207.

37 C. Xie, P. You, Z. K. Liu, L. Li and F. Yan, *Light: Sci. Appl.*, 2017, **6**, e17023.